

# Online Unsupervised Wildfire Detection Using Satellite Imagery

Steven Xu

*SAS Institute Inc.*

Cary, North Carolina, 27513 USA

Steven.Xu@sas.com

Seunghyun Kong

*SAS Institute Inc.*

Cary, North Carolina, 27513 USA

Seunghyun.Kong@sas.com

Zohreh Asgharzadeh

*SAS Institute Inc.*

Cary, North Carolina, 27513 USA

Zohreh.Asgharzadeh@sas.com

**Abstract**—We propose an unsupervised wildfire detection algorithm for multispectral satellite images. Our proposed algorithm is inspired by the observation that wildfire pixels often appear as sparse outliers residing in a spatially correlated infrared background. By recognizing the similarity between wildfire detection and infrared small target detection, we consider recovering the sparse component of the observation image using robust principal component analysis (RPCA). A novel cloud masking approach using histogram-based thresholding method is also proposed to improve the specificity of the detection algorithm. Compared to existing methods, our proposed method can adapt to the spatial and temporal heterogeneity of satellite images. It also does not require training on labeled images and is computationally efficient enough to be used in an online setting. Compared to traditional infrared small target detection methods such as background differencing, our proposed method is superior in both sensitivity and specificity. Compared to contextual cloud masking, our proposed histogram-based cloud masking is more accurate in binarizing cloud and wildfire pixels. By using a delayed detection technique, our proposed algorithm can take advantage of satellite images with high temporal resolution to detect active wildfires in a timely fashion while detecting few false alarms. As a demonstration, we apply the proposed algorithm to the GOES-R imagery to detect and monitor recent wildfires in California.

**Index Terms**—Unsupervised learning, RPCA, wildfire detection, multispectral imagery, image thresholding

## I. INTRODUCTION

Wildfire, or biomass burning, plays a significant role in an ecosystem as a sign of renewal and change. However, if uncontrolled, they can also bring irreversible damage to both human communities and the environment. At a local scale, unexpected wildfire poses serious threats to valuable assets and human safety. At a global scale, wildfires precede emission of greenhouse gas and particles, which in great quantity and can have long-term negative impacts on the Earth’s climate and public health [1]. In recent decades, wildfires in the western U.S. are increasing in frequency and duration [2]. In 2018, 7,948 incidents of wildfire were reported in California, charring an estimated 1,975,086 acres of land and causing hundreds of billions of dollars in losses. Despite various efforts, prevention of uncharacteristically large wildfires remains infeasible. Thus, detection and monitoring of wildfires have become paramount objectives in minimizing the economic and environmental costs. Early detection of wildfires ensures that suppression personnel can arrive on the scene when the fire is

still small and manageable, whereas real-time monitoring can provide timely information on the spreading trend and status change of active wildfires.

To date, notification of active wildfires relies mostly on human spotter reports. However, their effectiveness is limited to wildfires that happen during the daytime in populated areas, and their timeliness is usually difficult to determine quantitatively. To overcome these challenges, satellite images have been considered as an alternative resolution to provide valuable information on wildfires happening during nighttime or in regions where human presence is sparse [3]. Launched satellites usually fall in one of the two categories: Earth-orbiting and geostationary. The former monitors Earth dynamics on a global basis, while the latter captures continuous imagery of a fixed region. Early attempts to detect or monitor wildfires using satellite images, however, did not produce satisfactory results [4]. This is because satellite design in the past involved heavy resolution tradeoffs, and none of the launched satellites were designed specifically for fire detection. Earth-orbiting satellites, although equipped with high spatial resolution sensors, make infrequent passes over the same region on Earth. Geostationary satellites, although providing frequent snapshots of the same region, can only acquire coarse images because of the high altitude at which they are located.

Fortunately, recent years have witnessed a rapid advancement in remote sensing in terms of spatial resolution for geostationary satellites, and many new sensor systems have been deployed to provide new opportunities to enhance wildfire management [5]–[7]. The Geostationary Operational Environmental Satellites (GOES)-R series [8], for example, is the newest generation of weather satellites operated by NASA and the National Oceanic and Atmospheric Administration (NOAA) to provide advanced imagery and atmospheric measurements of Earth’s weather, oceans, and environment. Its current operations consist of GOES-16 and GOES-17 which were launched in 2017 and 2019, respectively. The two satellites provide rapid scans of the western hemisphere through 16 spectral bands covering visible and infrared wavelengths. The multispectral image data collected by GOES-R, with their high temporal resolution, are primarily used for online detection and monitoring of severe meteorological phenomena and natural hazards such as hurricanes, heavy rainfall, volcanic eruptions, and wildfires.

One of the most common approaches to detect active wildfire using multispectral images is to look for an intense response of spectral radiance at shortwave infrared (SWIR) wavelengths [4]. SWIR is characterized by a strong sensitivity to subpixel heat; therefore the sudden increase in earth surface temperature due to active wildfire signals a sharp increase in emitted radiance. Detection based only on data from SWIR wavelengths, however, can result in many false alarms. This is because solar reflectance during daytime makes the background warm, and a single-band threshold that separates warm background and wildfire often has a bad generalization across time and space. Alternatively, one can compare the emitted radiance at SWIR wavelengths to that at longwave infrared (LWIR) wavelengths. This approach uses the fact that SWIR has a more rapid response than LWIR to increasing heat. Compared to using SWIR measures only, this approach is more robust against warm background pixels because LWIR senses the actual near-ground temperature of the pixels being scanned. By calculating the differences between temperatures at SWIR wavelengths and LWIR wavelengths, one can classify pixels with close-to-zero difference as background and pixels with large positive difference as potential wildfires. In Fig. 1, the functional relationship between Planck's radiance and infrared wavelength is plotted for different temperatures. The more rapid response of SWIR to increasing heat is clearly observed.

Indeed, many fire detection methods proposed over the past decades rely on detection of the emitted radiance from wildfire in SWIR and LWIR wavelengths [9], [10]. These methods are typically classified into two categories: multi-channel thresholding algorithms and contextual algorithms. Multi-channel thresholding algorithms, as the name implies, directly use thresholds on a combination of infrared bands to binarize pixels into wildfire or background. Contextual algorithms, on the other hand, consider the local neighborhood of the scanned pixels and put thresholds on derived statistics that account for variation in the background environmental temperature. Most of these methods base their decisions on only two spectral bands: one at SWIR wavelengths and one at LWIR wavelengths, and the thresholds are often optimized for a specific sensor in a particular scenario that do not take into account the heterogeneity across global environments. One exception is [11], where the authors proposed to use the squared Mahalanobis distance in multispectral feature space to discriminate wildfire pixels. Their method incorporates radiance information from 15 spectral bands into a one-dimensional statistic that can adapt to global environments. More recent proposals have adopted state-of-the-art machine learning algorithms from the computer vision domain to solve the fire detection problem [12], [13]. For example, [14] considered training deep convolutional neural nets on remote images to segment fire or smoke pixels from the natural background. One drawback of these methods is that they require training over a large sample of labeled images to learn the specific characteristics of smoke or fire.

Infrared small target detection is another major application

of satellite imagery. In such problems, the target often has substantially higher brightness and appears isolated from surrounding background pixels that are spatially correlated. Thus, if we consider the original infrared image as a superposition of low-rank and sparse images, separation of the target from the background can be achieved by recovering the sparse component of the original image [15], [16]. It is not hard to see that the problem of wildfire detection shares many similarities with infrared small target detection, since typical wildfire pixels are substantially brighter than and appear isolated from the background pixels.

A common method to recover the sparse component of a data matrix is robust principal component analysis (RPCA) [17], [18]. RPCA assumes that the data matrix has an intrinsic low-rank structure that is corrupted by sparse outliers, and it solves the decomposition problem using tractable convex optimization. RPCA is commonly used in computer vision problems [18], [19] where either the low-rank or sparse component is of interest. For example, in face recognition, images of human faces have a low-dimensional structure, whereas the sparse matrix would contain self-shadowing or saturation in brightness; in video surveillance, the fixed background frames have a low-dimensional structure, whereas the sparse matrix would contain the moving objects. Recently, RPCA has also become a popular building block for infrared small target detection models. Some representative applications include defense technology [20] in which missile is separated from the sky background and cirrus cloud detection [21] in which clouds are separated from the earth background.

In this paper, a new method to detect and monitor wildfires online using machine learning algorithm is introduced. Our detection is primarily based on infrared images of brightness temperature (BT) difference, which is a nonlinear transformation of Plank's radiance, between a single LWIR band and a single SWIR band. By observing that wildfire pixels often appear as isolated bright dots in these infrared images, and background pixels are dim and spatially correlated, we adopted concepts from infrared small target detection and propose to decompose the given infrared image into low-rank and sparse components using RPCA. The potential wildfire pixels can be discriminated by locating the nonzero entries in the resulting sparse image matrix. In real applications, however, the sparse matrix from RPCA is often corrupted by noise. For an infrared target detection problem, the sparse matrix can also be corrupted by clutters. Therefore, it is crucial to apply a sequence of post-processing procedures to the direct sparse output to reduce the detection of false alarm. We showed that noise can be removed by placing a fixed threshold, whereas clutter can be removed based on its distinctive characteristics in the considered infrared bands. Our method offers a novel and simple solution to detect and monitor wildfires using multispectral satellite images. Compared with previously proposed approaches, it comes with several advantages. First, the thresholds used in our method are not optimized for individual scenarios and are robust to variations in global environments. Second, our algorithm is

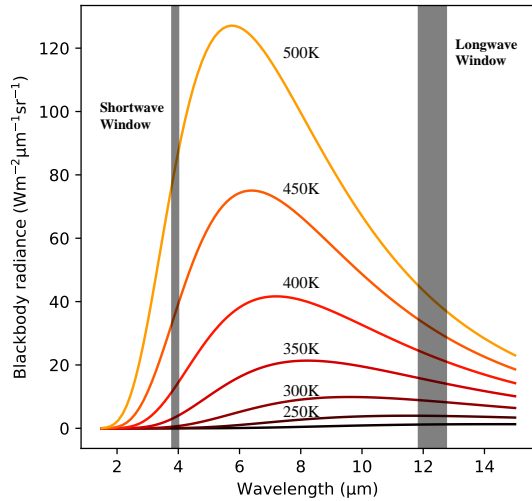


Fig. 1: Comparison of Planck radiances at shortwave window band vs longwave window band of GOES-R. The plot illustrates the more rapid response of the shortwave window band to increasing heat.

fully unsupervised and does not require pre-training on a large sample of labeled images. Last but not least, our algorithm is computationally efficient enough to run within seconds, thus making online monitoring of wildfires using satellite images with high temporal resolution practical.

The rest of the paper is organized as follows. We first introduce the data used in this work in Section II because many details of our method depends on specific features of this data set. The detection algorithm based on RPCA along with post-processing methods are introduced in Section III. Some preliminary results of our method are presented in Section IV, and comparison is made with existing methods on detecting and monitoring 2019 California fires using GOES-R imagery. Finally, we provide concluding remarks in Section V.

## II. DATA

The wildfire detection and monitoring algorithm proposed in this paper is based on features obtained from the GEOS-R multispectral images. Although our method can be easily modified to use imagery from other satellites or remote sensors, investigation in this direction is beyond the scope of this paper. There are many data repositories that store GEOS-R image data, such as NOAA, Google Cloud, Amazon Simple Storage Service (S3), and so on. In our analysis, we use data from Amazon S3 [22]. In this repository, a real-time feed and a historical archive of two GOES-R instruments are stored: Advanced Baseline Imager (ABI) and Cloud and Moisture Imagery (CMI). ABI images contain the geospatial radiance information with three coverage regions: full disk, which covers the western hemisphere; CONUS, which covers an approximately  $3000 \text{ km} \times 5000 \text{ km}$  area of the continental U.S.; and Mesoscale, which covers specific areas of the U.S. In our work we use CONUS images to monitor wildfires in the state of California since nearly every sizable wildfire is tracked by the local government and its agency. For instance, the

California Department of Forestry and Fire Protection stores detailed information such as location, duration, starting time and containment time of every sizable wildfire. As a result, we have documented evidence to validate fire detection methods. However, it is possible to apply our method to full disk images as well if research interest lies in detecting wildfires in remote areas, such as the Amazon rainforest.

The CONUS images are taken every 5 minutes and include 16 spectral bands. In our analysis we used 2 bands: the “short-wave window” band with a central wavelength of  $3.9 \mu\text{m}$ , and “dirty” longwave window band with a central wavelength of  $12.3 \mu\text{m}$ . Apart from the Plank’s radiance, which is directly available from the data set, we also calculated the brightness temperature (BT) of each band using the formula from the GOES-R document [23].

## III. METHODS

Suppose we are given an image with  $m$  rows by  $n$  columns of pixels. Each pixel of the image is characterized by numerous features, such as emitted radiance at the 16 spectral bands and any relevant transformations. Consider two specific features: brightness temperature (BT) at the  $3.9 \mu\text{m}$  band and  $12.3 \mu\text{m}$  band, and let  $\mathbf{T}_{3.9}, \mathbf{T}_{12.3} \in \mathbb{R}^{m \times n}$  denote the data matrices containing the respective features of the scanned pixels. Finally, let  $\mathbf{Y}$  denote the data matrix whose entries are calculated by subtracting the  $12.3\text{-}\mu\text{m}$  BT from the  $3.9 \mu\text{m}$  BT for each pixel; i.e.,  $\mathbf{Y} = \mathbf{T}_{3.9} - \mathbf{T}_{12.3}$ . Since the  $3.9 \mu\text{m}$  band is more sensitive to increasing subpixel heat than the  $12.3 \mu\text{m}$  band, the BT difference between the two bands will be significantly higher for wildfire pixels than for background pixels. Moreover, we can assume that with appropriate resolution, the number of wildfire pixels is substantially smaller than the total number of pixels in the given image. A visual example is shown in Fig. 2, where we project a sample BT difference image in Northern California onto the Lat/Lon coordinate. We see that genuine wildfire pixels have significantly higher BT difference than the background. If we store the BT difference of only the wildfire pixels in a data matrix  $\mathbf{S}$  of the same dimension as  $\mathbf{Y}$ , then we should expect  $\mathbf{S}$  to be sparse. The infrared background, on the other hand, consists of pixels whose BT difference is spatially correlated. That is, adjacent pixels in the image tend to have similar characteristics. If we represent the BT difference of infrared background with a data matrix  $\mathbf{L}$  of same dimension as  $\mathbf{Y}$ , then we should expect the columns of  $\mathbf{L}$  to be correlated. To summarize, we can assume that the BT difference matrix  $\mathbf{Y}$  is the superposition of a sparse matrix  $\mathbf{S}$  that contains the wildfire pixels and a low-rank matrix  $\mathbf{L}$  that contains the background pixels; i.e.,  $\mathbf{Y} = \mathbf{L} + \mathbf{S}$  (see Fig. 3 for an illustration). Under this assumption, wildfire detection is equivalent to recovering the sparse component  $\mathbf{S}$  based on  $\mathbf{Y}$  and checking for nonzero entries in  $\mathbf{S}$ . Wildfire monitoring can be achieved using similar steps. Assume we are not given a single but instead a stream of GOES-R images. Let  $\mathbf{Y}_t$ ,  $t = 1, 2, \dots$  be the constructed data matrix of each frame. Monitoring is equivalent to recovering the sequence of

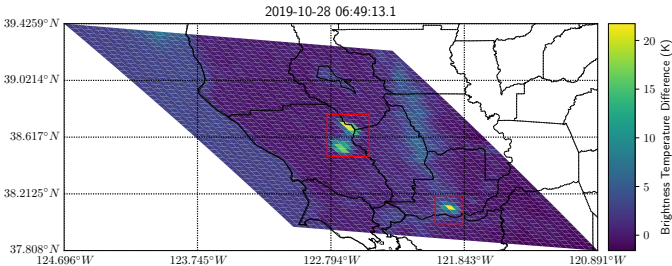


Fig. 2: An infrared image representing the brightness temperature (BT) difference of scanned pixels. The original image has been projected onto Lat/Lon coordinate. Areas in the bounding boxes represent approximate locations of confirmed wildfires. The plot illustrates that genuine wildfire pixels have a higher BT difference than the background.

sparse components  $S_t$ ,  $t = 1, 2, \dots$  and checking for nonzero entries in each of them.

#### A. Robust Principle Component Analysis

Principal component analysis (PCA) is often used to recover the low-dimensional structure of a data matrix with linearly correlated columns. However, when some entries of the data matrix are grossly corrupted by outliers, the recovered low-dimensional structure can be arbitrarily far from truth. To alleviate this problem, robust principal component analysis (RPCA) is proposed [18]. It assumes that the data matrix  $\mathbf{Y}$  can be decomposed into a low-rank matrix  $\mathbf{L}$  and a sparse matrix  $\mathbf{S}$ , where nonzero entries of the latter contain the outliers. Although RPCA was originally designed as a robust extension to PCA for dimension reduction objectives, in many applications the outliers in the sparse matrix  $\mathbf{S}$  are of interest. This is the case for our problem, as our primary objective is to detect potential wildfire pixels rather than recovering the infrared background. RPCA solves the decomposition problem through a two-objective optimization problem,

$$\min_{\mathbf{L}, \mathbf{S}} \text{rank}(\mathbf{L}) + \lambda \|\mathbf{S}\|_0 \text{ s.t. } \mathbf{Y} = \mathbf{L} + \mathbf{S} \quad (1)$$

where  $\text{rank}(\mathbf{L})$  represents the rank of matrix  $\mathbf{L}$ ; and  $\|\mathbf{S}\|_0$  represents the  $\ell_0$ -norm of matrix  $\mathbf{S}$ , which is just the number of nonzero entries  $\sum_{i,j}^{m,n} \mathbf{1}(S_{i,j} \neq 0)$ . The optimization problem in (1) is NP-hard, and therefore it is often transformed to the tractable convex optimization problem

$$\min_{\mathbf{L}, \mathbf{S}} \|\mathbf{L}\|_* + \lambda \|\mathbf{S}\|_1 \text{ s.t. } \mathbf{Y} = \mathbf{L} + \mathbf{S} \quad (2)$$

where  $\|\mathbf{L}\|_*$  is the nuclear norm of matrix  $\mathbf{L}$ , which is just the sum of eigenvalues  $\sum_i \sigma_i(\mathbf{L})$ , and  $\|\mathbf{S}\|_1$  is the  $\ell_1$ -norm of the matrix  $\mathbf{S}$ . The penalty coefficient  $\lambda$  controls the sparsity of  $\mathbf{S}$ . Specifically, larger  $\lambda$  will result in  $\mathbf{S}$  having higher sparsity. In the original RPCA paper [18], it has been proved that for an  $m \times n$  matrix under surprisingly broad conditions, the choice of penalty coefficient  $\lambda = \frac{1}{\sqrt{\max(m, n)}}$  can exactly recover the low-rank and sparse components. Many methods exist to solve the above convex optimization problem, such as augmented Lagrange multipliers (ALM) [24], accelerated proximal gradient (APG) [25], alternating direction method of

multipliers (ADMM) [26], etc. In our work, we use ALM to solve RPCA because of its simplicity and efficiency.

One rather limiting assumption that RPCA makes is that the low-rank component is exactly low-rank and the sparse component is exactly sparse. This assumption is almost always violated in real-world applications because the observations might be corrupted by stochastic or deterministic noise that affects every entry of the data matrix. A particularly problematic consequence can occur when RPCA is used in applications in which the sparse matrix  $\mathbf{S}$  contains the information of interest, since the resulting  $\mathbf{S}$  will contain not only the information of interest but also noise. If uncared for, the noise can make the outlier detection algorithm based on  $\mathbf{S}$  overly sensitive. To overcome this inconvenience, a stable variant of RPCA [27] was proposed to decompose the data matrix  $\mathbf{Y}$  into  $\mathbf{L}$ ,  $\mathbf{S}$ , and a noise component  $\mathbf{E}$  by solving a more complex optimization problem. However, this extra computational cost can be unappealing in an online setting, where execution time of the detection algorithm should be minimized.

In an image analysis context,  $\mathbf{S}$  might also contain clutter. Clutter is uninteresting objects in the image that have characteristics similar to those of the target. In our wildfire detection problem, the clutter is clouds, since they also have a significantly higher BT at  $3.9 \mu\text{m}$  and  $12.3 \mu\text{m}$  bands. Together with noise, they can detect a significant number of false alarms when the sparse matrix  $\mathbf{S}$  is directly used for detection. To overcome this challenge, we introduce an automatic approach to screen out cloud pixels using histogram-based thresholding which is described in Section III-B. We also provide a simple solution to remove noise by using a global image threshold which is described in Section III-C.

#### B. Cloud Masking Using T-point Thresholding

The characteristics of a cloud pixel in the sparse image  $\mathbf{S}$  is very similar to that of an actual wildfire pixel: both appear as bright dots with a high BT difference. This makes binarization of wildfire and cloud pixels using the BT difference image extremely difficult. To overcome this problem, we need to find a feature in which wildfire and cloud pixels are well separated. One feature that has such a property is the spectral radiance at the  $12.3 \mu\text{m}$  band, denoted as  $R_{12.3}$ . Water vapor absorbs atmospheric energy at  $12.3 \mu\text{m}$ ; therefore objects with high moisture, such as clouds, are significantly cooler than the infrared background in the  $12.3 \mu\text{m}$  band [28]. Using this information, we can identify a pixel in  $\mathbf{S}$  as a cloud if its  $R_{12.3}$  is significantly low. However, what qualifies as “significantly low” does not have a straightforward criterion. Compared to the characteristics of noise, which is relatively consistent across spatial and temporal domains, the patterns of clouds can vary dramatically across different scenarios. Therefore, a global threshold that is constant across space and time will yield poor results. Instead, the ideal thresholding technique should not only consider the averaged characteristics of cloud pixels but also allow for spatial and temporal variations.

In order to find an adaptive cutoff value that account for the distinctive characteristics of cloud pixels, we consider thresh-

olding based on the density function of  $R_{12.3}$  of the  $m \times n$  image. As mentioned before, cloud emits significantly lower  $R_{12.3}$  than the infrared background. If we were to visualize the density function, we should expect it to be approximately unimodal, with a major peak at high radiance representing the background as the main population and a heavy lower tail representing the cloud pixels with substantially lower radiance. Therefore, one way to screen out cloud pixels is to find the cutoff radiance value that well separates the lower tail and bulk of the pixel density.

The T-point algorithm [29] is an automatic image thresholding method based on the pixel density function. It assumes that the pixel density can be approximated by a unimodal histogram with a heavy upper tail. The histogram can be decomposed into three parts: a steep rising slope, a steep descending slope, and a slow descending slope. It then searches for the cutoff value automatically by fitting two regression lines, one for the steep descending and the other for the low descending slope, connected by one knot. The cutoff value that optimally separates the higher tail and bulk of the pixel density is set equivalent to the knot that minimizes the fitting error of the two regression lines. The original authors suggested minimizing the mean squared error (MSE), which is equivalent to fitting a piecewise least-square regression. However, MSE is known to be sensitive to outliers and noise. To make the optimal cut-off point more robust against erratic settings, we recommend minimizing the mean absolute error (MAE), which is equivalent to fitting a piecewise median regression. To see how the T-point algorithm can be used to screen out cloud pixels, let  $r$  denote a vector that stores the sorted negative pixel  $R_{12.3}$  of an  $m \times n$  image in ascending order. If cloud pixels contribute to the lower tail of the radiance density, then they will contribute to the higher tail of the negative radiance density. Let  $r_{(i)}$ ,  $i \in [1, mn]$  be the negative pixel radiance at the  $i$ th index. If we assume that the peak of radiance histogram has been identified at index  $p$ , then the T-point algorithm finds the optimal cutoff index  $t \in [p + 1, mn - 1]$  by solving the optimization problem

$$t = \arg \min \left\{ \sum_{i=p}^t |r_{(i)} - \hat{r}_{(i)}| + \sum_{i=t}^{mn} |r_{(i)} - \hat{r}_{(i)}| \right\} \quad (3)$$

where  $\hat{r}$  is the estimated radiance value by either of the two regression lines. Following (3), the optimal cutoff value that separates the higher tail and bulk of the negative radiance density is  $r_{(t)}$ . Thus we will identify a pixel as wildfire only if it satisfies the condition  $R_{12.3} > -r_{(t)}$ . A visual illustration of the T-point thresholding method is shown in Fig. 4, where the BT difference image,  $R_{12.3}$  image, and histogram of  $-R_{12.3}$  are plotted. We see that cloud pixels appear bright in the BT difference image but dark in the  $R_{12.3}$  image. The histogram of  $-R_{12.3}$  is unimodal with a heavy upper tail, and the steep descending slope and slow descending slope can be modeled with a piecewise linear regression.

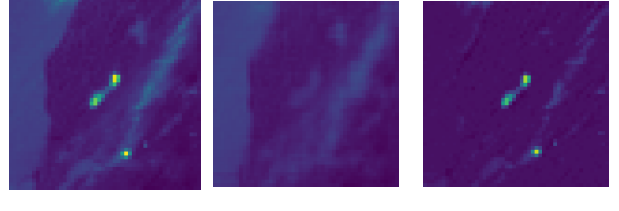


Fig. 3: Decomposition of a brightness temperature difference image into low-rank and sparse components. (a) The original image  $Y$ . (b) The low-rank image representing the spatially correlated background. (c) The sparse image representing potential wildfire with outlying pixel value.

### C. Noise Reduction

To reduce noise, we propose to apply Gaussian smoothing and a time-independent threshold to the direct sparse output  $S$ . We observe that noise in  $S$  appears as scattered and dim pixels with a BT difference lower than that of wildfire pixels. These are often the results of a warm background that emits terrestrial radiation and reflects solar radiation during the daytime. A low-pass filter is suitable for attenuating high-frequency noise while having little effect on the low-frequency signal. Gaussian smoothing is a low-pass filter that is widely used for reducing noise in images. It replaces the value of each pixel by the weighted average of its neighbor pixels. Since the noise pixels are scattered and dim, Gaussian smoothing will pull their values even closer to 0, whereas the values of wildfire pixels will stay relatively the same. The performance of Gaussian smoothing is dependent on the scale parameter that is used to select the size of the neighborhood. Intuitively, we would like to choose a small scale parameter so that attenuation is minimal for wildfire pixels. We also do not want it to be so small that Gaussian smoothing becomes meaningless. In this analysis, a scale parameter of 0.25 is chosen, and we defer the search for an automatic method for selecting this parameter to future work. After Gaussian smoothing, the pixel values of noise and wildfire will be well separated, and thresholding using a global cutoff value can be applied to screen out the noise. In this analysis, we propose to identify a pixel in  $S$  as a potential wildfire pixel only if it satisfies the condition  $T_{3.9} - T_{12.3} > 6K$ . Although this choice of cutoff value seems subjective, we will show in our experiment that it is robust enough against spatial and temporal heterogeneity.

The post-processing techniques described in this section are capable of screening out non-fire pixels across a broad settings. However, it is still possible to encounter settings in which some cloud or noise pixels might remain in the final sparse image. To further reduce the possibility of raising false alarms under these settings, we can take advantage of the high temporal resolution of GOES-R imagery and employ a delayed detection technique. That is, we classify pixels with nonzero values in an individual image as fire pixels only if they persist to be nonzero in a prespecified number of subsequent images. The number of subsequent images, or the delayed detection window size, can be treated as a tuning parameter and set

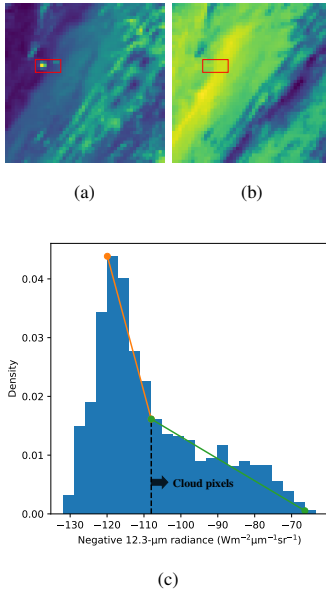


Fig. 4: Screening out cloud pixels using T-point thresholding algorithm. Red bounding box encloses the confirmed fire location. (a) The image containing brightness temperature difference of scanned pixels, bright pixels outside the red bounding box are contributed by clouds. (b) The image containing 12.3  $\mu\text{m}$  radiance of scanned pixels. (c) The histogram of negative pixel radiance. The fitted piecewise regression lines as well as the optimal cutoff value are also visualized.

by balancing the sensitivity and specificity of the wildfire detection algorithm.

#### IV. PRELIMINARY RESULTS

In this section, we provide some preliminary results of using the proposed algorithm to detect and monitor wildfires that took place in the state of California. In 2019, a reported total of 7,860 wildfires occurred in California [30]. However, not all of them are detectable by GOES-R. This is because the infrared sensor equipped on GOES-R has a resolution of 2 km, which can overlook fires with a burned size less than 4  $\text{km}^2$  (approximately 988 acres). In this paper, we focus on two wildfires: the Kincade fire and the Walker fire. To justify the advantage of our proposed algorithm over traditional methods in the infrared small target detection literature, we compare our method to background difference method which we describe in Section IV-A. We also demonstrate the competitiveness of the proposed cloud masking method by comparing it to a contextual thresholding method which we describe in Section IV-B. The results from applying our method and each of the competing methods to detect the Kincade fire and Walker fire are presented in Sections IV-C and IV-D, respectively.

##### A. Background Difference Method

Unlike our proposed method, which aims at recovering the sparse component of an individual image, the background difference method focuses on learning the low-rank structure of the underlying fixed or dynamic background for a sequence of images [31]. First, reference backgrounds are calculated by training on a set of “normal” images in which the target is not

present. The reference backgrounds are then used to estimate each background of a sequence of testing images in which the target is potentially present. Finally, the predicted backgrounds are subtracted from the testing images to obtain the residual images, based on which detection decisions are made. Coincidentally enough, RPCA is a widely used background difference method [32] for its ability to account for temporal heterogeneity in the backgrounds. This is a representative feature of satellite images, since the background is affected by varying lightness and weather throughout the day.

To detect and monitor wildfires online using the background difference method, let  $\{\tilde{\mathbf{Y}}\}_{i=1}^N \in \mathbb{R}^{m \times n}$  be a set of archived satellite images in which no wildfire is present. These images should cover a broad time range in order to account for the strong temporal heterogeneity of the background. Let  $\tilde{\mathbf{X}} \in \mathbb{R}^{N \times mn}$  be the data matrix constructed by row-stacking  $\{\tilde{\mathbf{Y}}\}_{i=1}^N$ , i.e.,

$$\tilde{\mathbf{X}} = \begin{pmatrix} \text{vec}(\tilde{\mathbf{Y}}_1) \\ \vdots \\ \text{vec}(\tilde{\mathbf{Y}}_N) \end{pmatrix}$$

where  $\text{vec}(\cdot)$  is the vectorization operator. The matrix that stacks the reference backgrounds can then be retrieved by recovering the low-rank component of  $\tilde{\mathbf{X}}$  using RPCA, which we denote as  $\tilde{\mathbf{L}}$ . Now suppose  $\mathbf{Y}_0$  is a real-time testing image in which an active wildfire is potentially present. We can estimate its background by projecting  $\mathbf{Y}_0$  to the row space of  $\tilde{\mathbf{L}}$ , i.e.,

$$\hat{\mathbf{L}}_0 = \text{vec}^{-1} \left( \mathbf{Y}_0 \tilde{\mathbf{V}} \tilde{\mathbf{V}}^T \right) \quad (4)$$

where  $\tilde{\mathbf{V}}$  are the right singular vectors of  $\tilde{\mathbf{L}}$  and  $\text{vec}^{-1}(\cdot)$  reshapes the result back to an  $m \times n$  matrix. That is, the estimated background is simply a weighted average of the reference backgrounds. The residual image  $\hat{\mathbf{D}}_0$  can then be calculated by subtracting  $\hat{\mathbf{L}}_0$  from  $\mathbf{Y}_0$ , and detection can be done by classifying a pixel with a value significantly greater than 0 as wildfire.  $\hat{\mathbf{D}}_0$  is often noisy, since the background cannot be perfectly approximated. It can also contain cloud pixels that contribute to false alarms. To have a fair comparison with the proposed method,  $\hat{\mathbf{D}}_0$  will be post-processed using the same techniques proposed in Section III-B and III-C. Since the proposed method and the background difference method are both based on RPCA, to avoid confusion we will refer to the former as frame-wise RPCA and the latter as RPCA background differencing in the rest of the paper.

##### B. Cloud Masking Using Contextual Thresholds

A cloud masking technique using a logic similar to that of our method was proposed in [11]. By acknowledging that cloud pixels appear dark in both 3.9  $\mu\text{m}$  and 12.3  $\mu\text{m}$  radiance, they suggested screening out cloud pixels by using contextual thresholds on these two features. In particular, they proposed to identify a pixel as a potential wildfire pixel only if it satisfies the condition

$$(R_{3.9} > \max\{\bar{R}_{3.9}, \bar{R}_{3.9}^l\}) \text{ and } (R_{12.3} > \max\{\bar{R}_{12.3}, \bar{R}_{12.3}^l\}) \quad (5)$$

where  $\bar{R}_{3.9}$  and  $\bar{R}_{12.3}$  are the average radiance of the full image in the two bands, and  $\bar{R}_{3.9}^l$  and  $\bar{R}_{12.3}^l$  are the average radiance of local windows in the two bands. One drawback of this method is that its result can be sensitive to the choice of local window size, which needs to be tuned for specific scenario. As will be shown in our experiment, a carelessly chosen window size can lead to poor detection performance, yielding higher false positive and lower true positive rates than our proposed method.

### C. Kincade Fire

The Kincade fire started October 23, 2019 in The Geysers as a result of a faulty electrical transmission line. It subsequently burned an area of 77,758 acres before it was fully contained on November 6, 2019. [30]. Image data that span the full 24-hour period of October 28, resulting in a total of 288 frames, were downloaded. During this time, the fire had already grown large enough and therefore was always detectable. The original resolution of the image covers an area of  $3000 \text{ km} \times 5000 \text{ km}$  that contains the continental U.S. To focus on the Kincade fire, we cropped a  $100 \text{ km} \times 100 \text{ km}$  region in Northern California; i.e., the dimension of each frame as a matrix is  $50 \times 50$ . It is worth mentioning that before seeing these images, we were only aware of the existence of the Kincade fire in the cropped region. However, during our analysis, we spotted a second cluster of persistently bright pixels that resemble a wildfire. After some online researching, we confirmed that the Grizzly Island fire [33] was also active on September 5. Hence in this experiment, we will provide results from detecting both the Kincade fire and the Grizzly Island fire.

To detect and monitor the Kincade fire using our proposed method, we apply RPCA to each of the 288 frames. For each of the resulting sparse images, the cloud pixels are removed using either the T-point or contextual thresholding method. For contextual thresholding method, a square local window with a side length of 5 is used throughout our analysis. Afterward, noise pixels are removed using the thresholding method proposed in Section III-C. For the background difference method, we obtain the reference backgrounds by training on images that span the full 72-hour period from October 19 to October 21, 2019. These dates are chosen because no sizable wildfire occurred at this time and they are temporally proximal to the testing images. The background of each each of the testing images is then estimated using (4) before subtraction is used to obtain the residual image. Finally, the residual images are post-processed using the techniques proposed in Sections III-B and III-C.

Visualized comparisons of a sample of five frames selected uniformly from the 24 hour period are shown in Fig. 5. For each frame and each method, we calculate the number of true positives (TP), which is the number of correctly identified fire pixels; and the number of false positives (FP), which is the number of non-fire pixels being classified as fire pixels. The number of false negatives is impossible to calculate, since we do not know the exact number of genuine wildfire pixels. We see that compared to the other two methods, our

proposed method identified more genuine wildfire pixels and successfully detected both the Kincade fire and the Grizzly Island fire in all five frames. In contrast, the contextual thresholding method and the RPCA background difference method failed to detect the Grizzly Island fire as demonstrated in Fig. 5(i) and Fig. 5(o), respectively. Two false alarms were detected by frame-wise RPCA in Fig. 5(a) and 5(f), but not by RPCA background difference method. However, the high degree of specificity of RPCA background difference method can not make up its low sensitivity, since the cost of missing a TP is significantly higher than detecting a FP when monitoring natural hazards. Furthermore, we will show that in an online monitoring setting, the false alarms can be avoided by employing a delayed detection.

### D. Walker Fire

The Walker fire started September 4, 2019 in Genesee Valley in the Plumas National Forest because of an unknown cause [30]. It was initially estimated to have a maximum size of 5 acres but later grew significantly because of strong and erratic winds [34]. It eventually burned up to 54,612 acres before it was fully contained on September 25, 2019. Image data that span the full 24-hour period of September 5 were downloaded. Based on online reports [34], the size of the Walker fire did not exceed the minimum detection limit before the evening of September 5. Therefore, the fire is detectable only in the later half of the downloaded frames. A  $100 \text{ km} \times 100 \text{ km}$  region in Northern California is again cropped as the training frame size, and fire detection and monitoring are applied using the same pipelines described in Section IV-C. For RPCA background difference method, we obtain the reference backgrounds by training on images that span the full 72-hour period from September 1 to September 3, 2019.

Visualized comparisons of a sample of five frames uniformly selected from the 24 hour period is shown in Fig. 6. The frames in the first two columns were captured when the Walker fire was still undetectable and therefore no wildfire pixel can be identified. Compared to the RPCA background difference method, the frame-wise RPCA method demonstrates a higher degree of both sensitivity and specificity. Compared to the contextual thresholding method, our proposed T-point thresholding method is superior in screening out cloud pixels and did not detect a single false alarm in all five frames.

As emphasized throughout the paper, our proposed method can be used to not only detect active wildfire in a single image, but also monitor formation or status change of wildfire in a real-time stream of images. The Walker fire data on September 5 is a great example to demonstrate the competitiveness of our proposed method in an online setting, since the size of the fire transitioned from being undetectable to being detectable by GOES-R (greater than  $4 \text{ km}^2$ ) in the evening of September 5 [34]. To demonstrate that our proposed method can detect this status change, we monitor the 288 downloaded frames assuming they are received in an online setting. The result of wildfire monitoring for a sample of six frames is shown

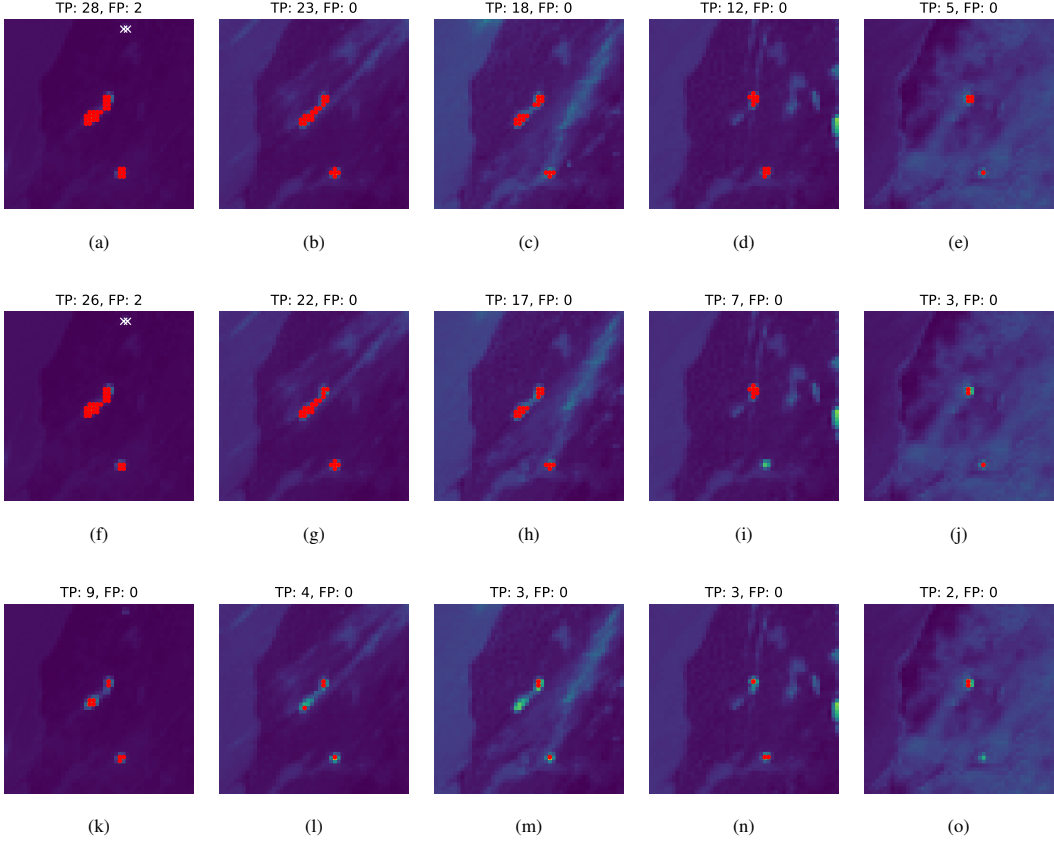


Fig. 5: Results of detecting the Kincade fire and Grizzly Island fire. Red dot represents correctly identified wildfire pixel and white cross represents false alarm. Number of true positives (TP) and false positives (FP) are calculated. (a)–(e) Result from frame-wise RPCA and T-point thresholding. (f)–(j) Result from frame-wise RPCA and contextual thresholding. (k)–(o) Result from RPCA background differencing and T-point thresholding.

in Fig. 7. These frames cover a short time range in which the Walker Fire is initially invisible in the BT difference image but later become visible. We see that genuine wildfire pixels are identified as early as 8:23 pm. However, false alarms are detected at 8:13 pm, 8:18 pm and 8:28 pm. As mentioned at the end of Section III, the specificity of our proposed detection algorithm can be further improved by using a delayed detection technique. In this experiment, we use delayed detection with a grace window of size 1. That is, we will only confirm the genuineness of a wildfire pixel observed in the current frame after observing it at the same location in the subsequent frame. If we apply delayed detection to the frames in Fig. 7, then potential fire pixels at 8:13 pm, 8:18 pm and 8:28 pm will not be confirmed as genuine fire pixels since they were not detected in the subsequent frames. As a result, we will be able to confirm our detection of the Walker fire at 8:28 pm without making any false alarms. According to documented evidence found online [34], the approximate time point when the size of Walker fire became detectable by GOES-R is between 7:25 pm and 8:55 pm, which is reasonably close to our result.

## V. CONCLUSION

In this paper, we proposed an unsupervised fire detection algorithm for multispectral satellite images using RPCA. Our

algorithm separates the sparse foreground that contributes to outlying wildfire pixels from the low-rank background. To reduce the possibility of raising false alarms, we also proposed to use a combination of image smoothing and thresholding methods to screen out noise and cloud pixels. Compared to existing fire detection algorithms, our proposed method demonstrates several advantages. First, it is very flexible and can adapt to the temporal and spatial heterogeneity of satellite images in different scenarios. Second, it is completely unsupervised and does not require pre-training on a large set of labeled images in order to yield accurate result. Last but not least, the proposed algorithm is computationally efficient and can run within seconds. The speed makes it suitable for online monitoring of wildfires using continuous imagery rather than making detection only in specific frames. We demonstrated the competitiveness of our proposed method by comparing it to the RPCA background difference method and the contextual cloud masking technique. Our method identifies more wildfire pixels and detects fewer false alarms in a variety of settings.

Our proposed method can be potentially improved in many ways as part of a future research direction. Currently, the parameters for Gaussian smoothing and global thresholding to screen out noise pixels are set manually. However, an automatic procedure to select these parameters will provide more

support to the generalizability of our model. Furthermore, we did not find a suitable performance metric that allows direct numerical comparison of our method to other existing methods. This is partly due to the limitation of GEOS-R imagery's spatial resolution and limited documented evidence that preclude us from locating the exact wildfire coordinates and validating the detection accuracy. In the future, we would also like to apply our method to satellite images from different sources so that a more comprehensive experiment can be designed to better show the competitiveness of our method.

## REFERENCES

- [1] P. Gupta, P. Doraiswamy, R. Levy, O. Pikelnaya, J. Maibach, B. Feenstra, A. Polidori, F. Kirov, and K. Mills, "Impact of California fires on local and regional air quality: The role of a low-cost sensor network and satellite observations," *GeoHealth*, vol. 2, no. 6, pp. 172–181, 2018.
- [2] X. Yue, L. J. Mickley, J. A. Logan, and J. O. Kaplan, "Ensemble projections of wildfire activity and carbonaceous aerosol concentrations over the western United States in the mid-21st century," *Atmospheric Environment*, vol. 77, pp. 767–780, 2013.
- [3] D. M. Szpakowski and J. L. Jensen, "A review of the applications of remote sensing in fire ecology," *Remote Sensing*, vol. 11, no. 22, p. 2638, 2019.
- [4] J. F. Weaver, D. Lindsey, D. Bikos, C. C. Schmidt, and E. Prins, "Fire detection using GOES rapid scan imagery," *Weather and Forecasting*, vol. 19, no. 3, pp. 496–510, 2004.
- [5] N. I. Sifakis, C. Iossifidis, C. Kontoes, and I. Keramitsoglou, "Wildfire detection and tracking over Greece using MSG-SEVIRI satellite data," *Remote sensing*, vol. 3, no. 3, pp. 524–538, 2011.
- [6] W. Schroeder, P. Oliva, L. Giglio, B. Quayle, E. Lorenz, and F. Morelli, "Active fire detection using Landsat-8/OLI data," *Remote sensing of environment*, vol. 185, pp. 210–220, 2016.
- [7] G. Xu and X. Zhong, "Real-time wildfire detection and tracking in Australia using geostationary satellite: Himawari-8," *Remote Sensing Letters*, vol. 8, no. 11, pp. 1052–1061, 2017.
- [8] Geostationary Operational Environmental Satellites - R Series, a collaborative NOAA & NASA program. Jul. 2012. [Online]. Available: <https://www.goes-r.gov/>
- [9] Y. J. Kaufman, C. O. Justice, L. P. Flynn, J. D. Kendall, E. M. Prins, L. Giglio, D. E. Ward, W. P. Menzel, and A. W. Setzer, "Potential global fire monitoring from EOS-MODIS," *Journal of Geophysical Research: Atmospheres*, vol. 103, no. D24, pp. 32 215–32 238, 1998.
- [10] V. Cuomo, R. Lasaponara, and V. Tramutoli, "Evaluation of a new satellite-based method for forest fire detection," *International Journal of Remote Sensing*, vol. 22, no. 9, pp. 1799–1826, 2001.
- [11] Y. Li, A. Vodacek, R. L. Kremens, and A. E. Ononye, "A new algorithm for global forest fire detection using multispectral images," in *Targets and Backgrounds IX: Characterization and Representation*, vol. 5075. International Society for Optics and Photonics, 2003, pp. 367–377.
- [12] J. Miller, K. Borne, B. Thomas, Z. Huang, and Y. Chi, "Automated wildfire detection through artificial neural networks," in *Remote Sensing and Modeling Applications to Wildland Fires*. Springer, 2013, pp. 293–304.
- [13] Z. Langford, J. Kumar, and F. Hoffman, "Wildfire mapping in interior Alaska using deep neural networks on imbalanced datasets," in *2018 IEEE International Conference on Data Mining Workshops (ICDMW)*. IEEE, 2018, pp. 770–778.
- [14] K. Govil, M. L. Welch, J. T. Ball, and C. R. Pennypacker, "Preliminary results from a wildfire detection system using deep learning on remote camera images," *Remote Sensing*, vol. 12, no. 1, p. 166, 2020.
- [15] Y. He, M. Li, J. Zhang, and Q. An, "Small infrared target detection based on low-rank and sparse representation," *Infrared Physics & Technology*, vol. 68, pp. 98–109, 2015.
- [16] H. Qin, J. Han, X. Yan, Q. Zeng, H. Zhou, J. Li, and Z. Chen, "Infrared small moving target detection using sparse representation-based image decomposition," *Infrared Physics & Technology*, vol. 76, pp. 148–156, 2016.
- [17] J. Wright, A. Ganesh, S. Rao, Y. Peng, and Y. Ma, "Robust principal component analysis: Exact recovery of corrupted low-rank matrices via convex optimization," in *Advances in neural information processing systems*, 2009, pp. 2080–2088.
- [18] E. J. Candès, X. Li, Y. Ma, and J. Wright, "Robust principal component analysis?" *Journal of the ACM (JACM)*, vol. 58, no. 3, pp. 1–37, 2011.
- [19] F. De la Torre and M. J. Black, "Robust principal component analysis for computer vision," in *Proceedings Eighth IEEE International Conference on Computer Vision. ICCV 2001*, vol. 1. IEEE, 2001, pp. 362–369.
- [20] Q. Chen, C. Wu, and Y. Wang, "Robust principal component analysis-based infrared small target detection," in *Proceedings of the AAAI Conference on Artificial Intelligence*, vol. 33, 2019, pp. 9925–9926.
- [21] Y. Lyu, L. Peng, T. Pu, C. Yang, J. Wang, and Z. Peng, "Cirrus detection based on RPCA and fractal dictionary learning in infrared imagery," *Remote Sensing*, vol. 12, no. 1, p. 142, 2020.
- [22] NOAA Geostationary Operational Environmental Satellites (GOES) 16 & 17. [Online]. Available: <https://registry.opendata.aws/noaa-goes/>
- [23] T. Schmit, M. Gunshor, G. Fu, T. Rink, K. Bah, W. Zhang, and W. Wolf, "GOES-R Advanced Baseline Imager (ABI) algorithm theoretical basis document for Cloud and Moisture Imagery Product (CMIP). Imagery.pdf." [Online]. Available: <https://www.star.nesdis.noaa.gov/goesr/docs/ATBD/Imagery.pdf>
- [24] Z. Lin, M. Chen, and Y. Ma, "The augmented Lagrange multiplier method for exact recovery of corrupted low-rank matrices," *arXiv preprint arXiv:1009.5055*, 2010.
- [25] Z. Lin, A. Ganesh, J. Wright, L. Wu, M. Chen, and Y. Ma, "Fast convex optimization algorithms for exact recovery of a corrupted low-rank matrix," *Coordinated Science Laboratory Report no. UILU-ENG-09-2214, DC-246*, 2009.
- [26] Q. Gu, Z. W. Wang, and H. Liu, "Low-rank and sparse structure pursuit via alternating minimization," in *Artificial Intelligence and Statistics*, 2016, pp. 600–609.
- [27] Z. Zhou, X. Li, J. Wright, E. Candes, and Y. Ma, "Stable principal component pursuit," in *2010 IEEE international symposium on information theory*. IEEE, 2010, pp. 1518–1522.
- [28] ABI band 15, quick guide. Aug. 2017. [Online]. Available: <https://www.goes-r.gov/mission/ABI-bands-quick-info.html>
- [29] N. Coudray, J.-L. Buessler, and J.-P. Urban, "Robust threshold estimation for images with unimodal histograms," *Pattern Recognition Letters*, vol. 31, no. 9, pp. 1010–1019, 2010.
- [30] Cal Fire. [Online]. Available: <https://www.fire.ca.gov/incidents>
- [31] H. Liu and X. Hou, "Moving detection research of background frame difference based on Gaussian model," in *2012 International Conference on Computer Science and Service System*. IEEE, 2012, pp. 258–261.
- [32] C. Guyon, T. Bouwmans, E.-h. Zahzah *et al.*, "Robust principal component analysis for background subtraction: Systematic evaluation and comparative analysis," *Principal component analysis*, vol. 10, pp. 223–238, 2012.
- [33] F. Kelliher, Grizzly Island fire scorches 2,300 acres, sends smoke across bay. Oct. 2019. [Online]. Available: <https://www.thereporter.com/2019/10/28/grizzly-island-fire-scorches-2300-acres-sends-smoke-across-bay/>
- [34] Walker fire day 3 updates. Sep. 2019. [Online]. Available: <https://www.plumasnews.com/walker-fire-day-3-updates/>

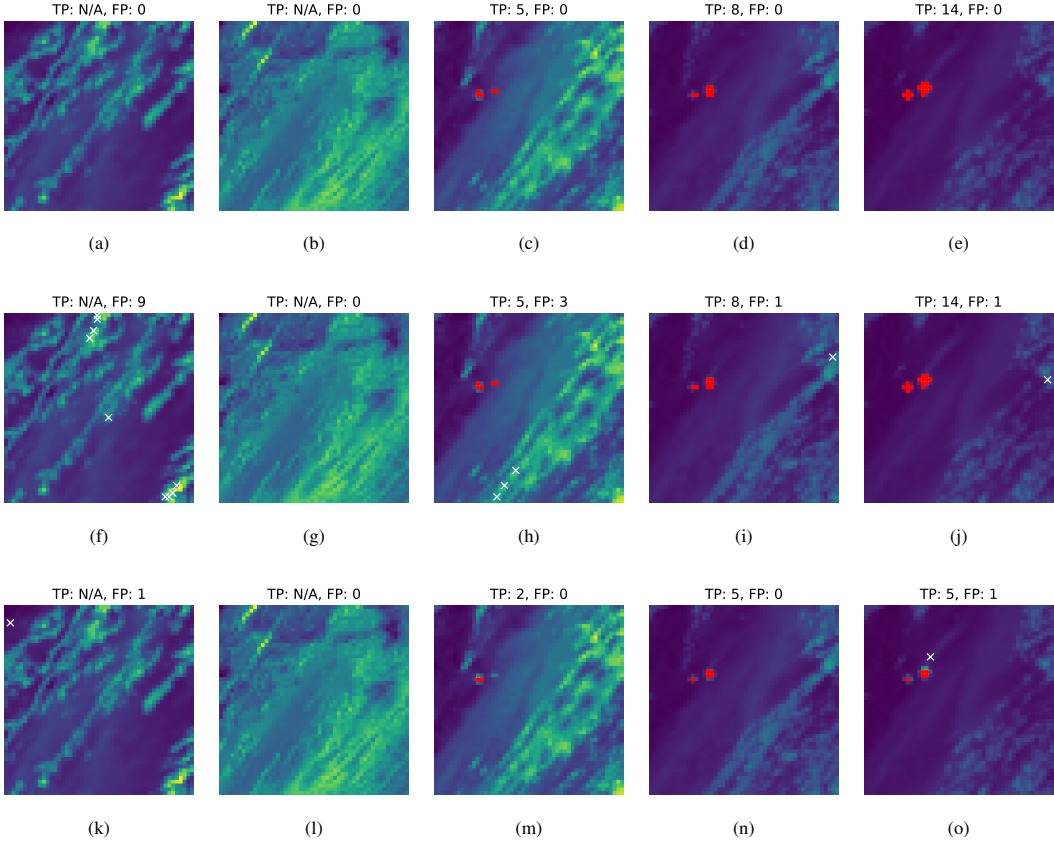


Fig. 6: Results of detecting the Walker fire. Red dot represents correctly identified wildfire pixel and white cross represents false alarm. Number of true positives (TP) and false positives (FP) are calculated. (a)–(e) Result from frame-wise RPCA and T-point thresholding. (f)–(j) Result from frame-wise RPCA and contextual thresholding. (k)–(o) Result from RPCA background differencing and T-point thresholding.

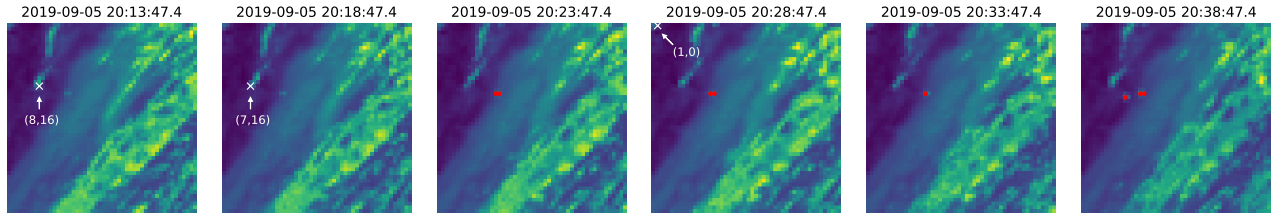


Fig. 7: Monitoring the Walker fire using frame-wise RPCA and T-point thresholding. Red dot represents correctly identified wildfire pixel and white cross represents false alarm. The  $(x, y)$  location of each false alarm, with  $(0, 0)$  representing the left top corner, is also shown.